

Hydrodynamics and Marine Optics during Cold Fronts at Santa Rosa Island, Florida

Timothy R. Keen[†] and Robert H. Stavn[‡]

[†]Oceanography Division
Naval Research Laboratory
Stennis Space Center, MS 39529, U.S.A.
timothy.keen@nrlssc.navy.mil

[‡]Department of Biology
University of North Carolina
Greensboro, NC 27402, U.S.A.



www.cerf-jcr.org



www.JCRonline.org

ABSTRACT

Keen, T.R. and Stavn, R.H., 2012. Hydrodynamics and marine optics during cold fronts at Santa Rosa Island, Florida. *Journal of Coastal Research*, 28(5), 1073-1087. Coconut Creek (Florida), ISSN 0749-0208.

Observations of optical and hydrodynamic processes were made on the open beach on Santa Rosa Island, Florida, in March 1995. This study focuses on the passage of two cold fronts. The observations have been supplemented by a bio-optical model; a suite of hydrodynamic models to simulate coastal flows forced by waves, tides, local wind, and coastal sea level; and a geo-optical model that predicts scattering by mineral particles resuspended by wave action. These models have been used to examine the interaction of atmospheric forcing and hydrodynamics with respect to the observed marine hydrosol. The optical and hydrodynamic measurements, and the model results, have been used to conceive a cold-front regime model of the hydrosol for open beaches in the Gulf of Mexico. The optical environment during the cold front was determined by three hydrosol phases: (1) a prefrontal steady-state hydrosol consisting of fine resuspended mineral particles, phytoplankton cells, organic detritus, and colored dissolved organic matter; (2) a frontal phase dominated by resuspended mineral particles; and (3) a postfrontal hydrosol containing large phytoplankton, detritus, and fine mineral particles. This concept is useful for identifying the physical processes responsible for observed optical properties. It should be applicable to other regions and types of events.

ADDITIONAL INDEX WORDS: Nearshore flow, waves, optical scattering, sand resuspension, marine hydrosol.

INTRODUCTION

The relationships between littoral hydrodynamics, the marine hydrosol (pure water, solutes, and small suspended particles), and the optical environment are fundamental to coastal sciences because of the widespread use of satellite-based instruments like the Moderate Resolution Imaging Spectroradiometer (MODIS) and the Medium Resolution Imaging Spectrometer (MERIS) (Acker *et al.*, 2009). The wide field of view and frequent overpasses of these sensors make them suitable for coastal morphology (Stockdon *et al.*, 2006), environmental studies (Hu *et al.*, 2005), and military applications (Hou *et al.*, 2007; Weidemann *et al.*, 2002). Instruments like the AC-9 spectrophotometer (Hakvoort and Doerffer, 1997) have been developed to collect ground-truth observations for calibration of remotely sensed observations. This requirement necessitates understanding the composition of the marine hydrosol. Validation studies are also useful for examining the interaction of hydrodynamic, sedimentation, and biological processes in coastal areas where comprehensive oceanographic data are often unavailable (Menon, Lotliker, and Nayak, 2006).

Background

In anticipation of the need to compare remote sensing with *in situ* optical data, oceanographic and optical field programs were completed at Santa Rosa Island (SRI), Florida (Figure 1), in August 1994 and March 1995 (Gould and Arnone, 1997). The 1995 data proved difficult to interpret, however, because of the interaction of physical, biological, and optical processes; the small area covered by the observations; and the impact of external forcing, which includes tides, coastal sea level changes (hereinafter coastal setup/setdown), and coastal upwelling/downwelling flows (Haus *et al.*, 2003; Keen and Glenn, 1994). These problems were exacerbated by multiple cold fronts that passed over the study area. Cold fronts are major environmental factors in the northern Gulf of Mexico in winter and spring (Feng and Li, 2010; Roberts *et al.*, 1987; Stone, 1998; Stone and Wang, 1999). They occur at a frequency of about one per week and impact the entire U.S. Gulf coast. They must, therefore, be considered in applying remote sensing methods to nearshore areas because of their impacts on the transport of both terrigenous and biological material by waves and currents. The rapidly changing wind fields during cold fronts produce waves, coastal setup/setdown, and current patterns that further complicate mass transport (Cobb, Keen, and Walker, 2008; Feng and Li, 2010; Keen, 2002; Keen *et al.*, 2003).

The SRI study has been followed by an ongoing research program to develop multicomponent optical models in littoral environments (Gould, Arnone, and Mueller, 1994; Haltrin *et al.*, 2007; Snyder *et al.*, 2008). Models of the littoral optical field

DOI: 10.2112/JCOASTRES-D-11-00179.1 received 26 September 2011; accepted in revision March 18, 2012.

Published Pre-print online 23 September 2012.

© Coastal Education & Research Foundation 2012

2012/228003

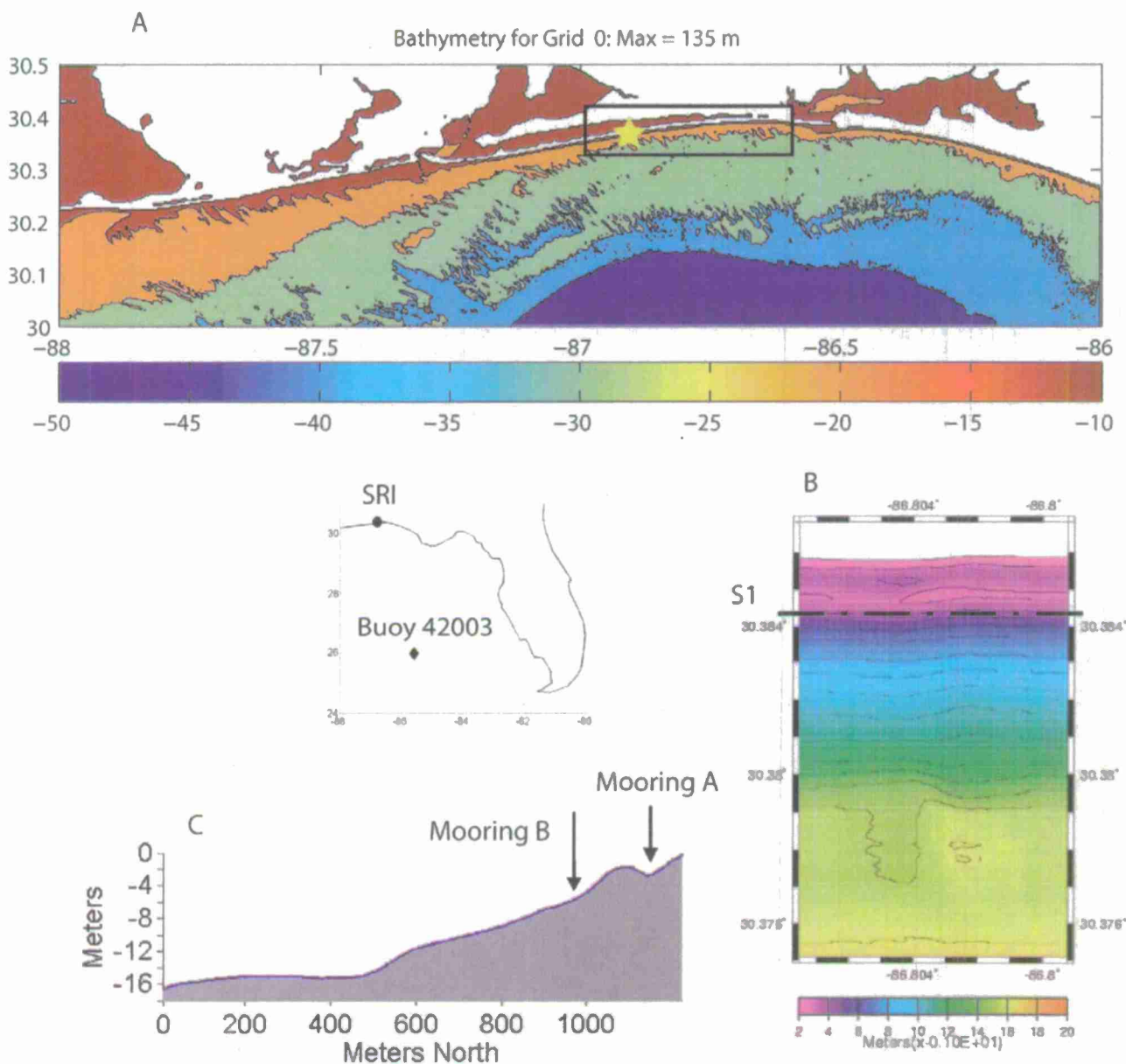


Figure 1. (A) Bathymetry for the 300-m NCOM grid. The location of the study area is indicated by a star. The local model (100 m) grid is outlined. (B) Bathymetry for the nearshore model at 1-m resolution. Section S1 refers to Figure 7. (C) Depth profile along the center of the field area (86.8035° W). Moorings A (30.385° N) and B (30.384° N) are discussed in the text. The inset map shows the location of the study area (circle) and buoy 42003 (diamond). (Color for this figure is only available in the online version of this paper.)

have helped identify the critical biological, geological, and oceanographic requirements for accurately predicting optical scattering in water depths shallower than 30 m on sandy coasts (Keen and Stavn, 2000; Ramnath *et al.*, 2010; Stavn and Keen, 2004). The predicted optical properties can be passed to optical-sensor models (McBride, Weidemann, and Shoemaker, 1999). This approach has been tested using the observations and model simulations for SRI (Keen, Stavn, and Kaihatu, 2006).

The results were inconclusive, however, because of the complex hydrodynamics during the March study period.

Objectives

This paper examines the interaction of hydrodynamic, sedimentation, biological, and optical processes at SRI using observations, in combination with numerical models. The

integration of these processes into a comprehensive model of the hydrosol at SRI is facilitated by the following conceptual model. The hydrosol at SRI can be divided into three regimes based on the hydrodynamics during a cold front: (1) a prefrontal steady-state hydrosol consisting of mineral particles, phytoplankton, organic detritus, and colored dissolved organic matter (CDOM); (2) a frontal hydrosol dominated by mineral particles resuspended by wave action; and (3) a postfrontal hydrosol comprising large phytoplankton cells, organic detritus, and small mineral particles.

This paper is organized in the following manner. "Methods" describes the observations collected at SRI in March 1995 and presents the bio-optical model that is applied, in addition to the numerical models for hydrodynamics and sediment resuspension. "Results" first presents the observations of hydrodynamics and the simulated flow. The optical measurements are then examined, and finally the hydrosol and optics model results are presented. We examine the interrelationships among atmospheric forcing, hydrodynamics, hydrosol composition, and optics with respect to the conceptual model in "Discussion."

METHODS

This work consists of three components: (1) oceanographic and optical data collected at SRI in March 1995; (2) a bio-optical model to estimate scattering by organic and inorganic particles, in addition to absorption spectra; and (3) a numerical modeling system to calculate hydrodynamics, mineral particle suspensions, and optical scattering by inorganic particles. This method of predicting the optical environment can be termed biogeo-optical (Stavn and Richter, 2008). The models comprising component 3 are necessary because it is not possible to incorporate the multiscales and multiphysics associated with the coupled hydrodynamic and optical environment in the coastal ocean. We thus use each of these models to examine a limited aspect of the problem.

Observations

Wind measurements from a meteorological buoy (Figure 2) revealed multiple cold fronts in March 1995. Cold fronts are identified by prefrontal southerly winds followed by a rapid change to postfrontal northerly winds. For example, the prefrontal wind blew from E-SE during 5 to 7 March, but its origin rotated to northerly immediately after the cold front on 8 March (hereinafter CF1) and remained so until 10 March. This paper refers to frontal passage as the period when the wind first has a northerly component (blowing offshore). The wind speed does not always increase during cold fronts; for example, the front that occurred on 16 March (hereinafter CF2) had a more complex history that did not include a strong postfrontal wind. The strongest winds were southerly during several later fronts as well.

Observations were made at SRI between 2 and 17 March as a follow-up to an earlier study (Gould and Arnone, 1997, 1998). The bathymetry (Figure 1B) was measured using an airborne light detection and ranging system. Moorings A (water depth = 2.7 m) and B (water depth = 4.8 m) were deployed landward and seaward of a nearshore bar at 30.385° N and 30.384° N,

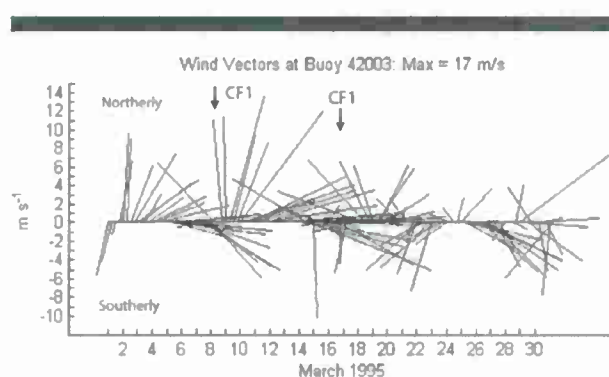


Figure 2. Feather plot of 6-hour winds subsampled from hourly measurements at NOAA buoy 42003 (25.966° N, 85.594° W), located 450 km south of SRI. The vectors point from the wind origin and terminate at the x-axis (e.g., southerly winds originate offshore). The approximate times of passage of the cold fronts discussed in the text are labeled CF1 and CF2. The maximum wind speed is calculated using all data.

respectively, and 86.8035° W (Figure 1C). The bottom gradient at mooring B is 0.018 in., but the seafloor has a 100-m-wide platform at a 15-m depth. The moorings were equipped with electromagnetic current meters near the surface and 1 meter above bottom (mab). WET Labs Inc. AC-9 spectrophotometers located at 1 mab measured total attenuation c_t and absorption a_t coefficients (in reciprocal meters) at optical wavelengths λ of 412, 440, 488, 514, 560, 630, 650, 676, and 715 nm. Mooring B included a bottom-mounted pressure sensor. Significant wave height (SWH) and period (SWP) were computed by spectral analysis of the unsmoothed measurements at a 10-minute sampling interval. Mean sea surface height (SSH) was computed as the variation from the mean of the time series. Ship-board measurements included chlorophyll-*a* concentration [Chl] using the fluorometric method along several across-shore transects in water depths of 2 to 7 m when weather permitted (Keen and Holland, 2010). These point measurements were grouped into surface (0–2.9 m), middepth (3–4 m), and bottom (4–6.1 m) averages.

Bio-Optical Model

The [Chl] is used to estimate the scattering from water, phytoplankton, bacteria, and organic detritus (Keen and Stavn, 2000). Total scattering is the sum of the contributing components (Mobley, 1994); therefore, we represent the particle scattering b_p measured by an instrument as a sum of organic and minerogenic particles (Peng *et al.*, 2007):

$$b_p = b_{ph} + b_d + b_q \quad (1)$$

where b_{ph} , b_d , and b_q are phytoplankton, organic detritus, and mineral (quartzlike) scattering, respectively. The total organic scattering, $b_o = b_{ph} + b_d$, can be estimated from [Chl]:

$$b_o = 0.21 \times [\text{Chl}]^{0.62} \quad (2)$$

Equation (2) was derived for case 1 ocean water (high phytoplankton compared to inorganic particles) at 550 nm, but it is used as an initial estimate for case 2 water (dominated

by inorganic particles) at SRI. We indicate total scattering estimated from spatial, temporal, or both mean values of [Chl] by $\langle b_o \rangle$. We convert the values from this equation to 440 nm with the following relation:

$$b_p(\lambda) \sim \lambda^{-1} \quad (3)$$

We can then estimate the scattering by mineral particles:

$$b_q = b_p - b_o \quad (4)$$

Equation (2) is used in the Naval Research Laboratory blue water model (Weidemann *et al.*, 1995). The estimated b_q is compared to the mineral scattering calculated by the geo-optical model.

The absorption spectrum can be represented by an exponential curve with a spectral slope S_X (Kirk, 1984):

$$a(\lambda) = a(\lambda_0) \exp(-S_X(\lambda - \lambda_0)) \quad (5)$$

The subscript X is d for detritus and C for CDOM. A reference wavelength λ_0 of 440 nm is used in our model. This relationship is used to test for the composition of the hydrosol using spectral scattering and absorption data from SRI. The appropriate values for the spectral slopes for detritus and CDOM, S_d and S_C , are taken from published reports.

Numerical Models

The flow landward of a nearshore bar is often assumed to be forced by surface waves, which may be ocean swell or locally generated wind waves. The open-coast site at SRI suggests that external factors like tides and coastal setup/setdown must be considered as well. To capture these physical scales of the hydrodynamics, this study uses a wave-forced hydrodynamic model for the nearshore flow and a general ocean circulation model for the lower shoreface and continental shelf. The currents from the hydrodynamic models are superimposed to incorporate all of these processes into the nearshore hydrodynamic regime. The resultant water depths and near-bed currents are used to drive a geo-optical model. The general system integration has been discussed elsewhere (Keen and Slingerland, 1993; Keen *et al.*, 2003). The interaction of wave-driven flow and steady currents (*e.g.*, tides) has a substantial impact on hydrodynamics for large waves (Rusu, 2010). This error is reasonable for this study because we are using observed wave properties rather than model predictions.

Hydrodynamic Modeling

The wind forcing for the hydrodynamic models was measured at National Oceanic and Atmospheric Administration (NOAA) buoy 42003 (Figure 2). Deep water and shelf currents are calculated using the Navy Coastal Ocean Model (NCOM). NCOM is a three-dimensional (3D) primitive-equation model that has been used for a number of littoral applications (Ko, Preller, and Martin, 2003; Morey *et al.*, 2003; Slingerland *et al.*, 2008). Subtidal currents, SSH, and 3D temperature and salinity fields for open boundaries and initial conditions are from the 1/8° global NCOM implementation (Barron *et al.*, 2004). These fields are passed to a regional model with a cell size of 300 m (Figure 1A). The astronomical tidal heights and mean transports are added along the open boundaries (Martin

et al., 2009). This model includes monthly climatological inflow for several rivers. The calculated currents, temperature, salinity, and water levels from the regional model are used as boundary conditions for a local NCOM grid with a cell size of 100 m (hereinafter the local model), which uses the same wind forcing but includes no rivers (Figure 1A). Variables used as boundary conditions are passed from the coarse nest to the finer nest (one-way coupling).

The wave-driven flow is computed using the quasi-3D Shorecirc hydrodynamic model (Haas *et al.*, 2003) on a grid with 10-m cells (Figure 1B), which is referred to hereinafter as the nearshore model. This model does not include wind or tidal forcing and uses periodic boundaries along the across-shore edges of the grid. It incorporates the Simulating Waves Nearshore wave model (Holthuijsen, Booij, and Bertotti, 1996) and can calculate local wave generation, in addition to propagating swell waves from offshore. The seaward wave boundary condition includes measured SWH and SWP from mooring B. The waves are assumed to approach the coast from directly offshore, because directional spectra were not measured. The resulting radiation stresses are summed over the wave spectrum and used for nearshore forcing of depth-averaged currents. Shorecirc includes both the standard and the roller-enhanced radiation stress inputs and a mass flux from Stokes drift and rollers to calculate the equilibrium undertow/3D current profile at each grid point (Haas and Warner, 2009).

Geo-Optical Model

The steady currents calculated from the nearshore (Shorecirc) and local (NCOM) hydrodynamic models are interpolated to 1 mab and superimposed to produce a steady current field above the wave boundary layer. Oscillatory currents are calculated from the measured SWH and SWP using linear wave theory.

The geo-optical model used in this study is the Littoral Sedimentation and Optics Model (LSOM), which incorporates a bottom boundary layer model (BBLM) for calculating wave-current shear stresses, bottom roughness, and suspended sediment profiles, in addition to a seafloor mass-conservation model (Keen and Slingerland, 1993). Input to LSOM includes SWH and SWP, wave direction, steady current speed and direction, water depth (including changes caused by tides, *etc.*), and the mean and standard deviation of a Gaussian size distribution describing the bottom sediment. The size distribution consists of 11 classes ranging from 0.023 to 1.05 mm; each size class has physical properties taken from previous studies (Glenn and Grant, 1987). The SRI simulations use a mean particle size $d_m = 156 \mu\text{m}$ (fine sand), with a representative critical shear stress of 14 dyne cm^{-2} and a settling velocity of 1.2 cm s^{-1} .

The concentration of sand grains in suspension predicted by LSOM depends on a number of parameters, including the resuspension coefficient γ_o , which has been estimated between 1.6×10^{-6} and 1.5×10^{-2} (Hill, Nowell, and Jumars, 1988; Keen and Stavn, 2000). These empirically determined values depend on the particle type and are thus valid for a given area.

LSOM includes a module that calculates scattering by quartz particles (b_{qs}) from the computed sediment distribution

(Haltrin *et al.*, 1999; Keen and Stavn, 2000). The scattering by a particular size class of quartz particles is determined in the module by the following:

$$b_{qg} = N\sigma_p = N\pi r^2 Q_{sc} \quad (6)$$

where N is the number of particles in a particular size class of resuspended sediment, σ_p is the scattering cross-section of the particle, r is the radius of the spherical equivalent of the particle, and Q_{sc} is the particle scattering efficiency calculated from Mie theory. When there are several size classes, subscripted with i , the scattering by the total quartz particles in suspension is

$$b_{qg} = \sum N_i \pi r_i^2 Q_{sc,i} \quad (7)$$

The LSOM module calculates quasi-3D fields of suspended sediment and scattering and resulting changes in bed height, but it is used to compute vertical profiles only for this study. The predicted scattering coefficients have been validated for a range of wave conditions on a sandy beach on the Pacific Coast of the United States (Stavn and Keen, 2004).

RESULTS

This section presents the observations and model results for the hydrodynamic and optical environments at SRI during the cold fronts in March 1995. More attention is paid to CF1, however, because of problems with the AC-9 instrument during CF2. Results from Equation (5) for hydrosol modeling are also presented. The hydrosol conceptual model is referenced to aid in the presentation of the results.

Hydrodynamics

This section presents the observations before and after each cold front separately. These pre- and postfrontal intervals are assigned based on meteorological measurements, which may not be reflected in other observations. The observations at moorings A and B are presented first. The hydrodynamic predictions from the local and nearshore models are then compared to the measurements at mooring B and used to examine the potential impact of regional hydrodynamics on the nearshore flow.

Observations

March began with a cold front (Figure 2), after which the wind rotated from N to SE and, by 6 March, had become the prefrontal wind of CF1. This southerly wind generated a coastal setup of approximately 30 cm by 8 March (Figure 3B) and a southerly ocean swell, with wave heights of about 1 m (Figure 3A) and periods of 3 to 8 seconds (not shown). The flow inside the bar was onshore in response to the wind and waves, and the surface currents (Figure 4A) were similar in magnitude to the bottom currents (Figure 4C). The surface flow outside the bar (Figure 5) was predominantly westward and less than 20 $\text{cm}\cdot\text{s}^{-1}$, with weak eastward flow during the flood tides of 4 and 5 March. Westward currents strengthened to 50 $\text{cm}\cdot\text{s}^{-1}$ by 7 March because of the persistent SE wind, which also generated SWH greater than 2.5 m. Plunging breakers were observed over the bar, and spilling breakers were seen landward.

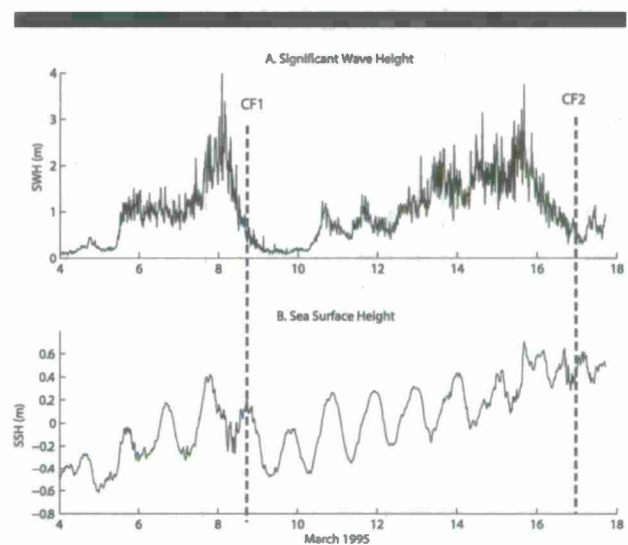


Figure 3. Measurements at mooring B: (A) SWH (in meters) and (B) SSH. See Figure 1 for location. The labels CF1 and CF2 are for the approximate times of the cold fronts discussed in the text.

Plunging breakers were also observed intermittently seaward of the bar (A. Weidemann, personal communication). Wave breaking probably contributed to the increased noise in SSH at mooring B (Figure 3B), which was more pronounced at low tides.

The onshore flow inside the bar strengthened to more than 40 $\text{cm}\cdot\text{s}^{-1}$ before 8 March because of the rising tide, large waves,

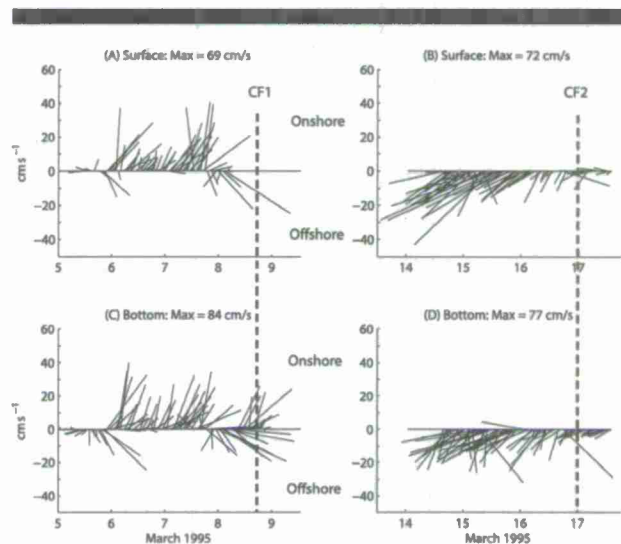


Figure 4. Measured currents at site A subsampled at 1 hour: (A) and (B) surface flow and (C) and (D) bottom currents. The instrument did not record between 9 and 14 March. See Figure 1 for location. The dashed lines indicate the cold fronts as identified from the winds at buoy 42003. The maximum values on the plots are computed from all data.

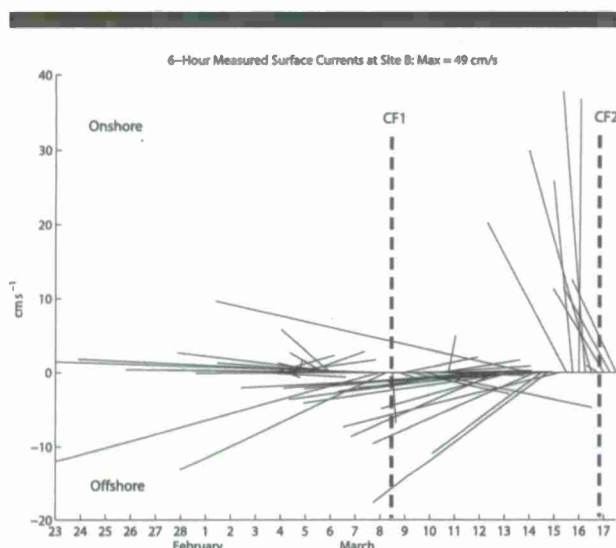


Figure 5. Feather plot of measured surface currents at mooring B. The original data were subsampled at 6-hour intervals to improve readability. The maximum was computed using all data. The vectors originate at the x-axis and point in the direction of the current.

and coastal setup. A seaward flow developed after SWH exceeded about 1.5 m, however, and surface currents reached 69 cm s^{-1} to S-SE on the morning of 8 March. Surface flow outside the bar (Figure 5) was directed SW with a peak current of 63 cm s^{-1} . This strong seaward flow may be partly attributable to a rip current that originated in the channel through the bar (Figure 1B). This current pattern is similar to that observed in laboratory rip currents (Haas and Svendsen, 2002), but with a stronger alongshore flow that would be absent in a wave tank. The wind became northerly around 1800 on 8 March as CF1 passed.

The prefrontal interval of CF2 began with the E-SE wind on 13 March (*i.e.*, a weak onshore component). The SWH was less than 20 cm during the prefrontal interval, but waves increased as the wind became more easterly between 10 and 13 March. A daily increase in SWH occurred because of a sea breeze that was not measured at the buoy. SSH began to rise on 13 March, while SWH exceeded 1 m as CF2 approached. The current measurements resumed inside the bar on 14 March, and flow was to the SW. The flow inside the bar was to the SW before CF2, with surface currents up to 72 cm s^{-1} (Figures 4B and D). The southerly wind exceeded 10 m s^{-1} on 15 March, and wave heights reached 2 m; breaking waves are suggested by the noisy SSH time series from mooring B (Figure 3B). The surface flow outside the bar was onshore on 15 March, with currents of 20 to 35 cm s^{-1} (Figure 5). The currents weakened inside the bar at this time but remained seaward, which is consistent with a rip current before CF2, but if one developed, it did not reach the seaward mooring.

Cold front CF2 passed over the study area around midnight on 16 March, as indicated by the wind rotating from S to NW.

This shift was accompanied by a steady decay of SWH to less than 50 cm. The postfrontal wind persisted until 21 March.

Simulated Combined Flow

The across-shore tidal current of about 5 cm s^{-1} (Figure 6A) is not apparent in the local model result because of currents forced by waves, wind, and coastal setup. The onshore flow before CF1, and seaward flow immediately after it, are reproduced—but with less noise than in the measurements. These currents are associated with the prefrontal coastal setup predicted by the model. The northerly wind on 9 March drives an offshore flow in the local model that is stronger than observed. This is probably an artifact of the 100-m grid, which has a constant water depth of 2 m this close to the coast. The local model predicts seaward flow after 11 March that is similar in magnitude to the measurements. The nearshore model predicts onshore currents of about 15 cm s^{-1} (Figure 6A) whenever SWH exceeds 1 m, which is in disagreement with both the measurements and the local model. It is likely caused by the onshore propagation of waves in Shorecirc when the wind is from the SE.

The local model responds to the SE wind by predicting westward surface currents of more than 30 cm s^{-1} at mooring B (Figure 6B). This flow weakens just before CF1, and an eastward flow is predicted on 8 March. When the wind returns to S-SE, however, westward alongshore flow resumes. This pattern is similar to the measured currents overall, but it has a much larger westward component than observed, which may be caused by the buoy winds. The simulated flow between 9 and 15 March has a phase error that may be caused by using the winds from the buoy. The nearshore model generates negligible alongshore currents.

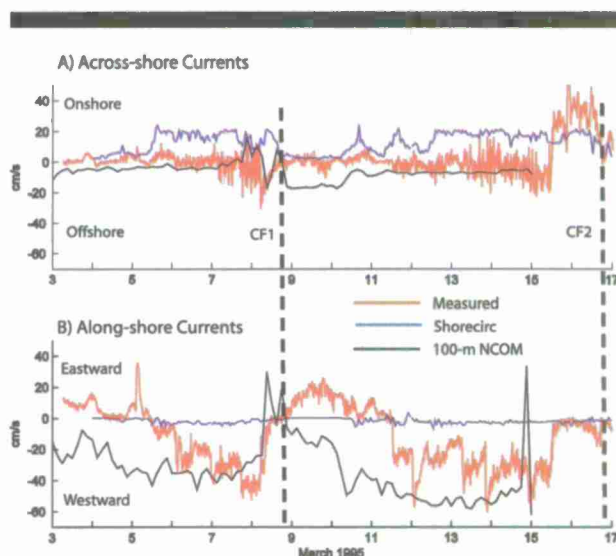


Figure 6. Surface currents at mooring B: observed (red), Shorecirc (blue), and 100-m NCOM (black) components for (A) the across-shore flow and (B) the alongshore flow. The local model results are from 30.3823° N , 86.8044° W .

The difficulty of simulating combined nearshore flows in an open-ocean environment with numerical models can be seen in this example. One approach to capturing the local and regional circulation is to introduce the radiation stress generated by waves into a general circulation model (Haas and Warner, 2009). This avoids the problem of representing different scales with different models, but it is limited in the extent of the model domain because of the need to resolve the nearshore bathymetry in the circulation model. For example, Haas and Warner (2009) used the Regional Ocean Modeling System to simulate an area similar in size to the nearshore domain of this study. For now, this remains a problem in simulating combined nearshore hydrodynamics.

The measured currents inside the bar before 1800 on 7 March were predominantly N-NE (Figure 4), while flow was westward seaward of the bar (Figure 5). The existence of a rip current just before CF1 would have contributed to currents within the study area (Figure 1B) for the 12 hours it persisted, but the open coast at SRI is also subjected to flow caused by coastal setup. The local model does not predict rip currents, which suggests that a substantial component of the observed westward flow (Figure 6) was forced by the coastal setup. This comparison indicates that the flow outside the bar was dominated by coastal-scale processes, and wave-driven impacts were restricted to rip currents and wave resuspension of seafloor sediments.

The predicted flow before CF1 (Figure 7A) is onshore at the surface and seaward at the bottom, whereas the entire water column has an offshore component 48 hours later (Figure 7B). The modeled alongshore currents are westward before CF1 (Figure 7C) because of the SE wind. The flow remains westward on 10 March but weakens substantially (Figure 7D). The combined flow during the prefrontal period reveals variability at the scale of the nearshore grid (10 m) because of wave-driven currents.

The E-SE wind before CF1 generates a coastal downwelling flow in the local model (Figure 8A), with surface currents as high as 90 cm s^{-1} . The simulated alongshore flow is westward throughout the water column (Figure 8B), while onshore surface currents of 40 cm s^{-1} are balanced by seaward bottom currents of 10 cm s^{-1} (Figure 8C). This downwelling flow persists until the northerly postfrontal wind pushes surface water offshore (Figure 9A). The resulting flow is westward (Figure 9B), with an alongshore jet exceeding 20 cm s^{-1} at the surface and eastward currents less than 10 cm s^{-1} near the bottom on the lower shoreface. Upwelling-favorable flow is indicated by near-bottom onshore currents greater than 10 cm s^{-1} (Figure 9C) that are offset by seaward surface currents of 30 cm s^{-1} . This flow field is in overall agreement with the observations at mooring B. It is also consistent with the expected downwelling and upwelling flow regimes associated with the wind.

Optical Measurements

Attenuation Coefficients

The measured beam attenuation and absorption coefficients can be used to estimate particle scattering from $b_\lambda = c_\lambda - a_\lambda$. Here, we use the subscript λ to indicate a spectral measure-

ment. The resulting b_{440} (Figure 10A) exceeded a_{440} (blue line) during most of the deployment. The attenuation peaks before CF1 are correlated with the inferred rip current discussed previously, but a_{440} remained elevated after b_{440} decreased at 1200 on 9 March. This sudden decrease may reflect an instrument malfunction or obstruction, because the measurements resumed midday on 10 March.

The phytoplankton absorption peak at 440 nm (Cleveland, 1995) is absent from the spectrum for 6 March (Figure 11), but the 650-nm tail is present. This spectrum is similar to the August 1994 spectra from SRI (Gould and Arnone, 1997). The blue end of the spectrum shows increased absorption on 9 and 10 March. These spectra resemble total suspended matter spectra for a hydrosol dominated by depigmented detritus (both organic and mineral) in the Pearl River, China (Hongyan *et al.*, 2007). Absorption remained high until 12 March (triangles), when weak phytoplankton absorption peaks at 440 and 650 nm are evident.

The spectral dependence of scattering coefficients from open-ocean (case 1) water can be parameterized by $b_L(\lambda) \approx \lambda^{-0.3}$ and $b_F(\lambda) \approx \lambda^{-1.7}$ for the large and fine fractions, respectively (Shifrin, 1983). The resulting trend is increased scattering at longer wavelengths and more scattering by the large fraction. In contrast, the spectral scattering coefficients on 6 March (Figure 12) increase at shorter wavelengths, which is the expected trend for case 2 water (Babin *et al.*, 2003; Wozniak and Stramski, 2004). This trend is similar to spectra from surface measurements in a water depth of 3 m from August 1994 (Gould and Arnone, 1997). The magnitudes of the March 1995 b_λ spectra from mooring B (water depth = 4.7 m) are intermediate between surface measurements at 3 and 8 m water depths in August 1994. Similar spectral dependencies were derived for other locations in the northern Gulf of Mexico where total scattering was partitioned into an organic component and a component due to suspensions of clay minerals (Stavn and Richter, 2008). This trend steepened on 8 March 1995 (Figure 12) when SWH exceeded 3 m, at which time b_λ increased from about 1 m^{-1} at 650 nm to 4.5 m^{-1} at 412 nm. This spectrum contains a small peak at 670 nm, which is in agreement with theoretical calculations and measurements of scattering spectra (Babin *et al.*, 2003; Stramski, Babin, and Wozniak, 2007). The b_λ spectra from 9 and 10 March (Figure 12) were similar to the case 1 trend, but scattering was much greater on 9 March. The spectrum on 12 March indicates a return to conditions before 8 March.

Chlorophyll

The mean [Chl] (Figure 10B) increased between 2 and 4 March and remained elevated until CF1. There was also an increase in [Chl] with depth on 4 March. The surface [Chl] on 6 March decreased by 23%, from 8.01 mg m^{-3} in the morning to 6.13 mg m^{-3} in the evening, which is indicative of diel variability (Yentsch and Ryther, 1957). These levels are typical of nonbloom conditions for case 2 water (Wozniak and Stramski, 2004). The surface [Chl] measurements on 9 March were more variable than before CF1, and they were slightly smaller. The surface [Chl] of 4.05 mg m^{-3} on 10 March indicates a 40% decrease during CF1. This may reflect a

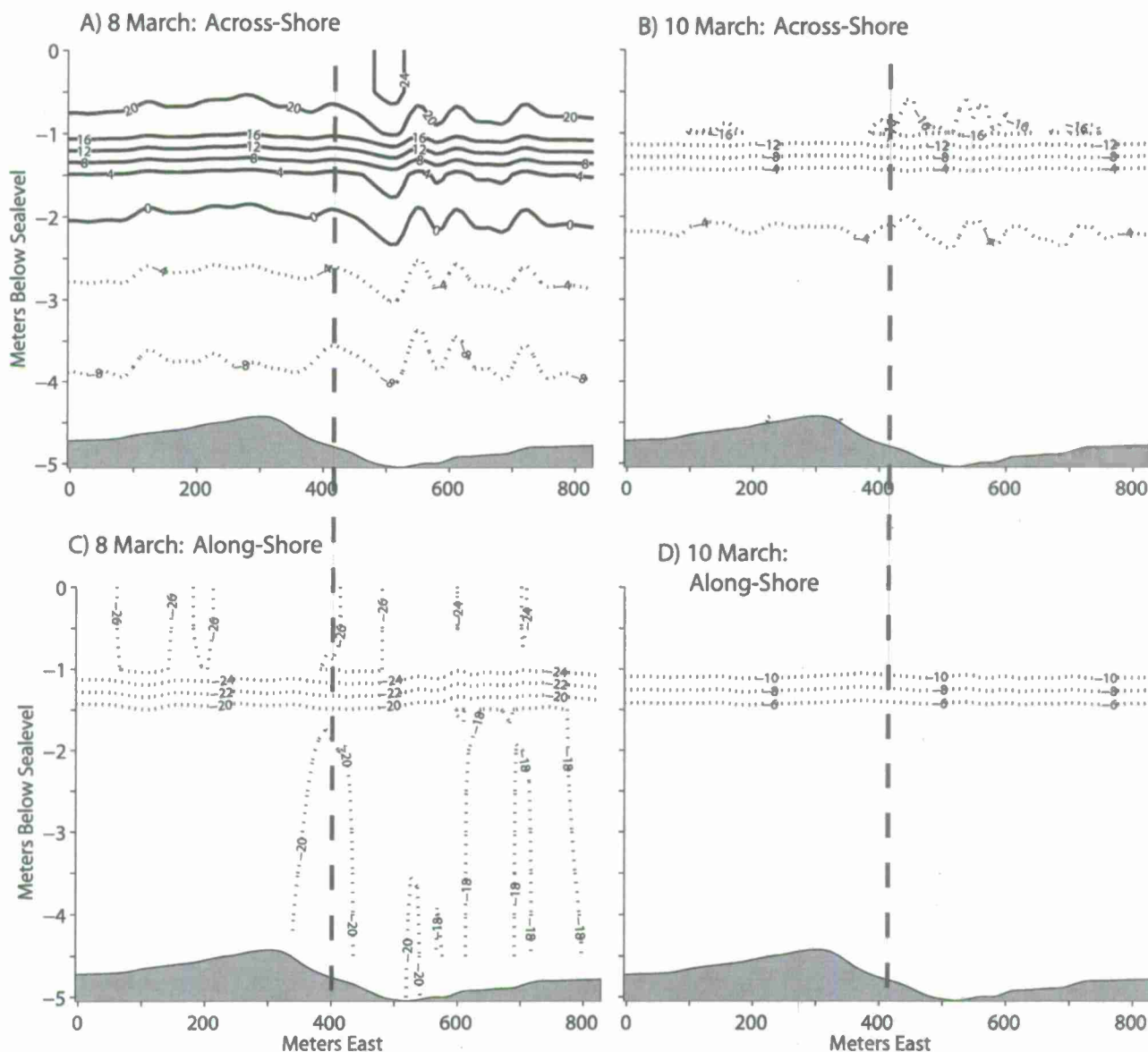


Figure 7. Cross-sections looking onshore of combined currents computed by nearshore and local models: (A) across-shore component on 8 March, 18 hours before CF1; (B) across-shore component on 10 March, 30 hours after CF1; (C) alongshore currents on 8 March; and (D) alongshore currents on 10 March. The section is outside the bar at 30.384° N, as shown in Figure 1B. The location of mooring B is indicated by the heavy dashed lines. Negative (dashed) contours are (C and D) westward and (A and B) offshore.

reduction in the number of cells or a shift in environmental conditions that favored a different phytoplankton community after the cold front (Tamigneaux *et al.*, 1999).

Hydrosol and Optics Modeling

An optical scatter sensor to directly measure b_o and b_q (Lee and Lewis, 2003) was not available for this study. Instead, we

estimate b_o from Equation (2), and b_q is then found from Equation (4). This section uses the bio-optical and geo-optical models to constrain the kinds of particles in the water at SRI. We focus on mooring B because the AC-9 instrument at mooring A was partially buried by sand during CF1 and the attenuation coefficients were too large to be useful for model comparison.

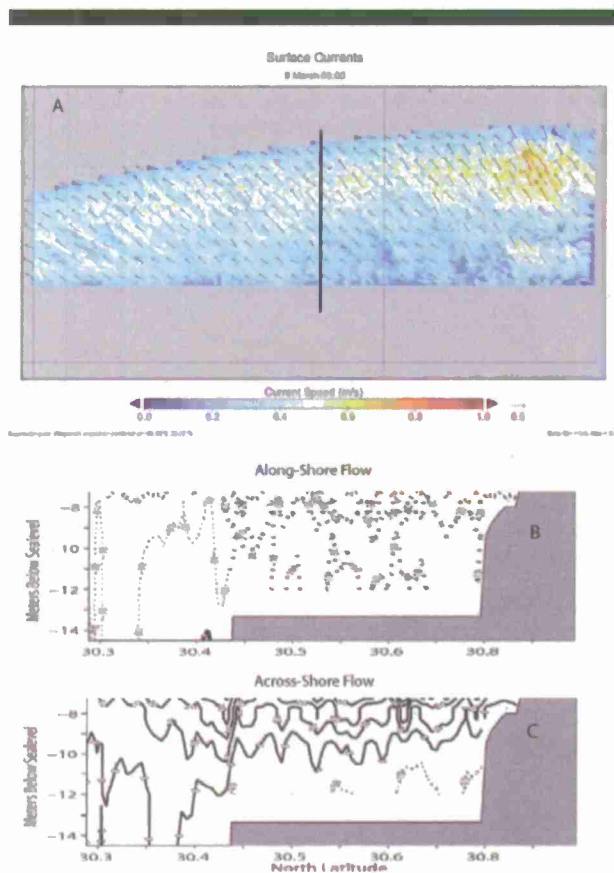


Figure 8. Snapshots of surface currents calculated by the local model (NCOM on the 100-m grid) on 8 March. (A) Equirectangular projection of surface current vectors over magnitude centered at 86.8° W, 30.33° N. The vectors are plotted for every 10th cell for clarity. The N-S sections looking west: (B) alongshore currents and (C) across-shore currents. Negative (dashed) contours are (B) westward and (C) offshore. (Color for this figure is only available in the online version of this paper.)

Scattering Estimated by the Bio-Optical Model

The total organic scattering b_o estimated from Equation (2) (Table 1) was less than 1 m^{-1} on 6 March; thus, b_q from Equation (4) was 2 to 3 m^{-1} . The average organic scattering $\langle b_o \rangle$ is more useful for 9 and 10 March because the measurements were so closely timed. The resulting ratio of minerogenic to organic scattering, b_q/b_o , which was 2.5 before CF1, peaked at 8.4 on 9 March before decreasing to 4.5 on 10 March. This large ratio indicates that the hydrosol contained substantial numbers of detrital particles. The large estimated ratio of minerogenic to organic scattering is consistent with b_{440} (Figure 10A), which was greater than 2 m^{-1} for most of the study interval. The bio-optical model results thus suggest that mineral particles prevailed in the water column throughout the observation period, including 9 March, when absorption was nearly as strong as scattering. This anomalous post-CF1 interval requires further examination, as does 8 March.

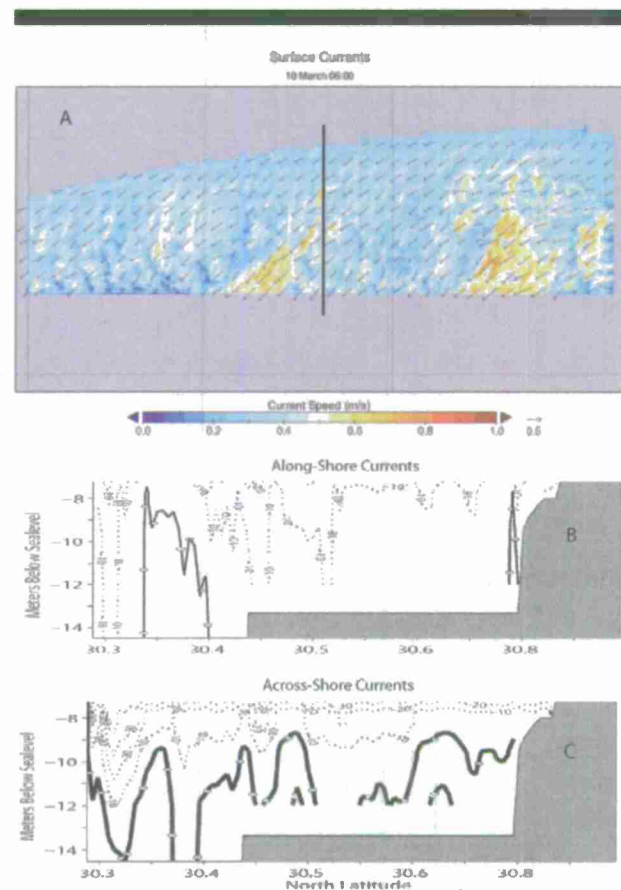


Figure 9. Snapshots of currents calculated by local model (NCOM on the 100-m grid) on 10 March. (A) Equirectangular projection of surface current vectors over magnitude centered at 86.8° W, 30.33° N. The vectors are plotted for every 10th cell for clarity. The N-S sections looking west: (B) alongshore currents and (C) across-shore currents. Negative (dashed) contours are (B) westward and (C) offshore. (Color for this figure is only available in the online version of this paper.)

Scattering by Resuspended Mineral Particles

The only calibration required for the geo-optical model in this study was selecting a value for the resuspension coefficient that produces a good fit of b_{qg} to b_{440} when both SWH and b_{440} were large—we use $\gamma_o = 2.3 \times 10^{-4}$. The predicted scattering b_{qg} at 0300 on 8 March (Figure 13) includes mean organic scattering $\langle b_o \rangle = 0.654 \text{ m}^{-1}$. The BBLM properties and resulting mineral scattering b_{qg} at mooring B were then calculated at 12-hour intervals between 7 and 11 March. Nonlinear effects from breaking waves are limited at this water depth for most waves (Camenen and Larson, 2007), although there were occasional large waves within the study area.

The total scattering, $b_{qg} + \langle b_o \rangle$, at 440 nm predicted by LSOM (Figure 13) is lower than the measured b_{440} between 8 and 11 March. It is possible that this error is caused by low combined currents predicted by the nearshore and local models. To examine this possibility, we also calculated the

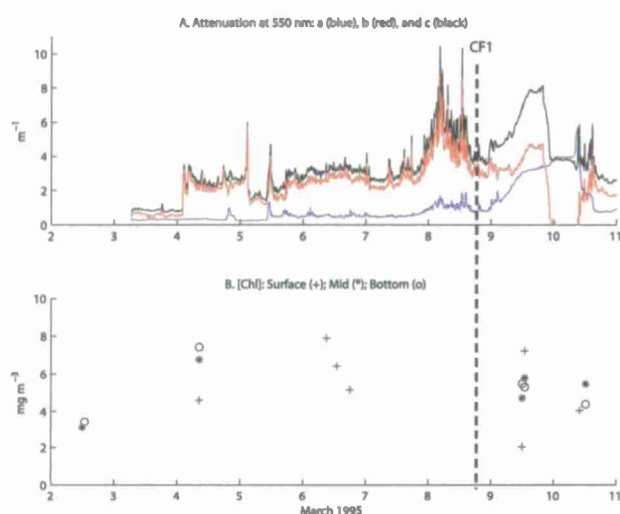


Figure 10. Optical measurements at mooring B in March 1995. (A) Coefficients (m^{-1}) for attenuation c_{440} (black line), scattering b_{440} (red line), and absorption a_{440} (blue line). The AC-9 sensor was located 1 mab. (B) The [Chl] (mg m^{-3}) measured near the mooring.

total scattering using the same geo-optical model parameters but using the measured surface currents at a reference height of 4.5 mab. The resulting scattering is similar to that using the model currents except on 8 March, when a possible rip current increased the surface magnitude significantly. The predicted scattering is nil when SWH is less than 0.75 m, at which time the predicted scattering is dominated by organic matter $\langle b_o \rangle$.

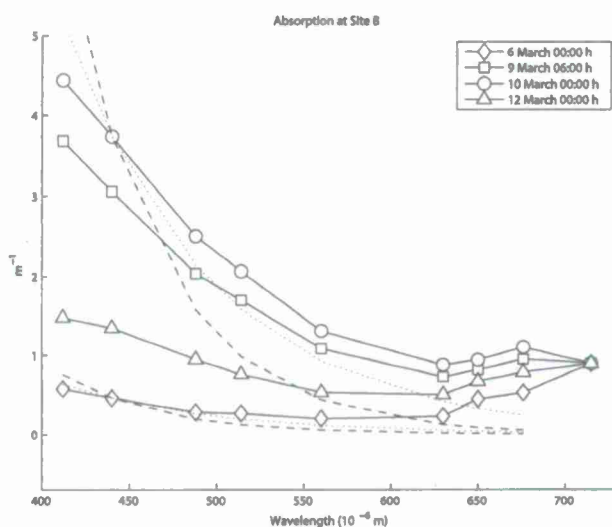


Figure 11. Measured absorption spectra at mooring B. The dashed lines are CDOM spectra calculated with Equation (5) using a slope parameter $S_C = 0.018$. The dotted lines are the modeled detritus spectra using $S_d = 0.0085$.

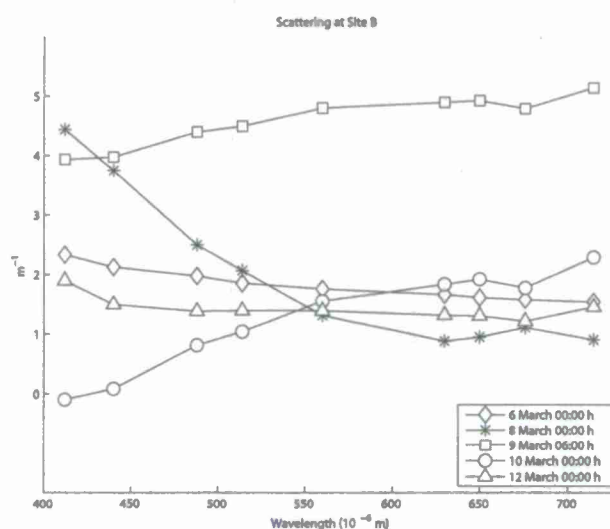


Figure 12. Measured scattering spectra at 1 mab at mooring B.

The low SWH and b_{gg} on 9 March indicate that the hydrosol was not dominated by resuspended mineral particles, as suggested by the bio-optical model. The low values of $\langle b_o \rangle$ further suggest that these particles were not living phytoplankton cells. The measured attenuation could have been caused by other materials, such as organic and inorganic detritus (Stavn and Richter, 2008), which would have been transported into the study area. The transport of sand particles is less likely for this water depth because of their high settling velocity, which would have required a continuous source of turbulence to keep them in suspension. This does not preclude small numbers of clay minerals and flocs in the hydrosol, however, which would have settling velocities on the order of 10^{-3} to $10^{-4} \text{ cm s}^{-1}$ (Fugate and Friedrichs, 2002).

Absorption Spectra

We can test for the presence of detritus and CDOM using Equation (5) with values of S_d and S_C , respectively, from the literature. The best-fit spectral slope S_d ($\lambda = 350\text{--}600 \text{ nm}$) for detritus near the Patagonia coast is 0.012 to 0.0083 nm^{-1} . (Ferreira, Garcia, and Garcia, 2009). Depigmented particles from the Pearl River, China, produced a slope of 0.0116 nm^{-1} . (Hongyan *et al.*, 2007). The SRI data are best fit with $S_d = 0.0085 \text{ nm}^{-1}$ (Figure 11). The fit is less good for λ greater than 626 nm . There remains some uncertainty in defining detritus, however, which may include organic and inorganic sources.

The value of S_C has been reported more often than that of S_d . Estimates of S_C in spring off Patagonia ranged from 0.011 to 0.019 nm^{-1} , whereas summer values ranged from 0.008 to 0.016 nm^{-1} . Values of 0.015 to 0.0185 nm^{-1} have been determined for the Pearl River (Cao *et al.*, 2003; Zhao *et al.*, 2009), as well as the South Atlantic Bight and North Sea (Kowalczyk *et al.*, 2003; Stedmon, Markager, and Kaas, 2000). S_C equal to 0.018 nm^{-1} results in a regression that is clearly inappropriate for the SRI data (Figure 11). We have not used

Table 1. Model-predicted scattering coefficients.

Day-Hour	b_o (m^{-1})	b_q (m^{-1})	b_{org} (m^{-1})	$(b_q - b_{org})$ (m^{-1})
06–1000	0.95	2.40	3.42	–1.02
06–1400	0.86	2.64	6.48	–3.84
06–1900	0.81	2.87	—	—
09–1300	0.77*	6.47	0.0	6.47
10–1100	0.69*	3.11	0.0048	3.105

* Calculated from the average of multiple [Chl] values, indicated by < b_o > in the text.

the estimates from the Pearl River, because they are believed to be contaminated by substantial anthropogenic and terrigenous input (Hongyan *et al.*, 2007). The hydrosol thus appears to contain less CDOM than detritus on 9 and 10 March. These results for absorption and scattering after CF1 bring into question the appropriate models for detritus and CDOM, but organic detritus should nevertheless have a lower spectral slope than CDOM (Ferreira, Garcia, and Garcia, 2009).

DISCUSSION

The hydrosol evolved during CF1 as a direct consequence of the combined impact of waves and currents on minerogenic sediments and the phytoplankton community. The optical signature of these interactions was blurred by other components of the marine hydrosol that are not well understood (*e.g.*, CDOM and organic detritus). We can shed light on these processes by examining the optical data with respect to the observations and model simulations.

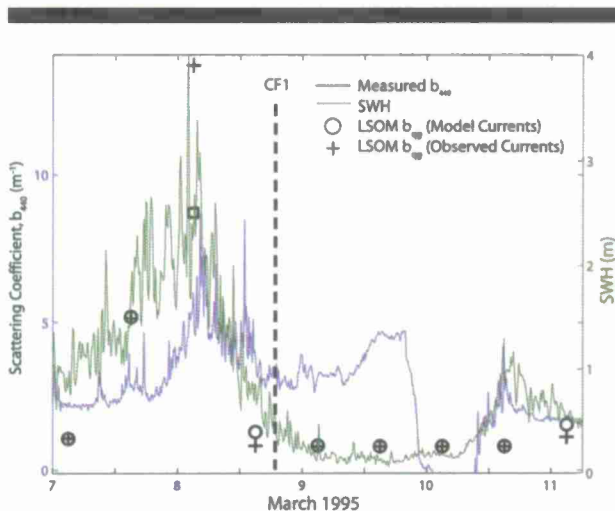


Figure 13. Time series for measured scatter coefficient at 440 nm (blue line) and SWH (green line) at mooring B during 7 to 11 March. The observed b_{440} data were measured at 10-minute intervals. The circles are the sum of the average organic scattering < b_o > and the predictions from LSOM (b_{org}) using the hydrodynamic forcing discussed in the text. The square indicates the time used to calibrate LSOM. Scattering using measured surface currents and waves is indicated by (+).

Hydrodynamic Regimes

It is tempting to think of the open coast at SRI as a steady-state, two-dimensional, hydrodynamic system (Power *et al.*, 2010). This idealized environment is characterized by southerly winds of less than $5 m \cdot s^{-1}$ and low swell (SWP < 6 s and SWH < 1 m). Currents in the surf zone consist of a westward flow of less than $10 cm \cdot s^{-1}$ and a variable wave-driven component of similar magnitude. Currents exceed $20 cm \cdot s^{-1}$ on the shoreface because the persistent SE wind and its associated coastal setup both contribute to a westward flow. This is a reasonable representation of the hydrodynamic regime in summer 1994 if no tropical cyclones are present in the Gulf of Mexico, as well as the observations at SRI for 4 to 7 March 1995. During winter and spring, it is convenient to refer to this quiescent “summer” hydrodynamic regime as prefrontal, from an oceanographic perspective. Turbulence is restricted to the vicinity of the nearshore bar and is highly variable.

The prefrontal hydrodynamic regime at SRI changed as the high-pressure system associated with CF1 approached and the wind speed increased. This synoptic wind field generated swell in the central Gulf, as well as local waves. The combined SWH greater than 3 m increased flow in the surf zone to approximately $40 cm \cdot s^{-1}$ before CF1, and rip currents were generated that extended seaward to mooring B. The regional flow during this hydrodynamic regime is reproduced by the local model (Figure 8), which predicts a downwelling flow on 8 March. This oceanographic frontal regime is easily identified by the SWH peaks on 8 and 15 March. Wave breaking was continuous over the bar and intermittent at mooring B. Turbulence levels were consequently quite high over the upper shoreface (Yoon and Cox, 2010).

The postfrontal hydrodynamic regime is defined by the northerly winds that occurred immediately after CF1. The northerly winds caused SWH to plummet and coastal sea level to fall rapidly. Turbulence levels in the surf zone and shoreface consequently decreased. The coastal current system during the postfrontal period was characterized by upwelling-favorable flow, as predicted by the local model on 10 March (Figure 9). The NE wind and falling coastal water levels combined to maintain a mean westward flow over the inner shelf during this interval.

Evolution of the Hydrosol

The primary components of the hydrosol at SRI are mineral particles (quartz and clays), organic detritus, phytoplankton (large and small), and CDOM (Stavn and Richter, 2008). The relative numbers of these constituents are determined by events and processes in a range of scales, including biological interaction, resuspension from the seabed, input from rivers, and transport by wave-driven, tidal, and steady currents. Although it is not possible to quantify all of these processes, we can examine their relative contributions to the optical environment during CF1 using the frontal hydrodynamic regime introduced in the previous section.

The hydrosol composition was fairly constant during the prefrontal interval. The large ratio of scattering to absorption (Figure 10A) indicates the importance of mineral particles and detritus. The absorption spectrum from 6 March 1995 (Figure

11) is similar to that from August 1994, and [Chl] remained below $8 \text{ mg} \cdot \text{m}^{-3}$, with no indication of a bloom event. The prefrontal a_λ distribution can be fit for both CDOM and detritus, and both may have been present. The geo-optical model results preclude the resuspension of mineral particles at mooring B for the low SWH during the prefrontal period—note the high b_{440} (Figure 10A) on 5 March 1995 when SWH was less than 30 cm. However, mineral grains resuspended in the surf zone would have been transported offshore by rip currents and undertow. Taken together, these hydrodynamic, optics, and sedimentation results indicate that the prefrontal hydrosol consisted of phytoplankton and organic detritus, as well as mineral particles and possibly CDOM.

The only optical measurements during the frontal hydrodynamic regime were attenuation spectra. Absorption (not shown) was similar to the prefrontal period, but the b_λ trend steepened while displaying the phytoplankton spike at 676 nm (Figure 12). The geo-optical model predicts that resuspended mineral particles would have been a major component of the hydrosol at this time. This interpretation is in agreement with observations and models of case 2 scattering (Gould, Arnone, and Martinolich, 1999). It is likely, however, that the phytoplankton community survived disruption by turbulence during the frontal phase while sand was resuspended all across the upper shoreface by wave-induced turbulence. Strong currents were also transporting particles both offshore and to the west, as well as from the east.

The hydrosol did not return to its prefrontal composition immediately following CF1. The a_λ on 9 and 10 March suggest that detritus was accumulating when SWH was low and resuspension was limited to the submarine bar (Figure 1C). Transport from the surf zone is implied by the local model results, however. The absorption spectra from this time are consistent with large phytoplankton (Wang *et al.*, 2010), and the spectral slope is reasonable for detritus but not CDOM. The spectral scattering b_λ reached a maximum on 9 March, with a trend similar to case 1 water. The small dips in $b(\lambda)$ at 440 and 676 nm are consistent with the presence of large phytoplankton (Stramski, Bricaud, and Morel, 2001). The reduction of b_λ on 10 March indicates that these large organic particles were removed from the water column. This interpretation is supported by a decrease in scattering while maintaining the spectral shape on 10 March (Figure 12). The simultaneous increase in a_λ between 9 and 10 March suggests that these high-scattering particles were replaced with a strongly absorbing component. The anomalous attenuation coefficients during the postfrontal phase were probably caused by large phytoplankton detritus and terrigenous material that were transported by the persistent westward alongshore coastal circulation.

The a_λ distribution on 12 March (Figure 11) resembles the prefrontal spectrum but with larger magnitudes and a visible knee at 440 nm. The b_λ coefficients are somewhat smaller than the prefrontal values, but the dips at 440 and 676 nm, associated with large phytoplankton, remain. It is not possible to infer the exact nature of these hydrosol constituents without more data on the optical properties of suspended particles (Binding, Bowers, and Mitchelson-Jacob, 2005) and on the

relative contribution of living and detrital organic particles in ocean waters (Stavn and Richter, 2008).

CONCLUSIONS

We have applied the prefrontal hydrodynamic regime concept to propose a typical hydrosol at SRI during summer and spring. This hydrosol consists of a mixed community of phytoplankton that is accompanied by CDOM, organic and inorganic detritus, and mineral particles. Changes in the hydrosol during CF1 were due not only to phytoplankton dynamics but also to transport of dissolved and particulate matter and resuspension of mineral particles from the bottom. Heterogeneities in the distribution of these components in the prefrontal hydrosol would have been either homogenized or intensified by advection. The observations from SRI could not be used to identify the interplay of physical and biological processes during CF1 because of these factors. Only the numerical hydrodynamic models allow us to recognize the potential impact of advection on the hydrosol.

We have used the hydrodynamic models to simulate the coastal-scale flow in the context of the synoptic scale of a cold front. This approach does not couple the optical signature of the atmospheric-oceanographic event, which can be observed from satellites, to the individual components of the hydrosol (Green, Gould, and Ko, 2008). It is simpler than the approach that has been implemented for shelf and open-ocean environments (Nakata and Doi, 2006), but it proved useful in other coastal studies (Song *et al.*, 2010). Our results extend previous process-based studies to the surf zone while including the larger scales through the boundary conditions applied to the local and nearshore models. The importance of waves and steady currents for mixing the hydrosol at scales of meters to kilometers has thus been demonstrated. An important result has been the analysis of the nearshore data from the moorings with respect to the synoptic scale of the atmospheric forcing.

Understanding the coastal remote sensing environment requires better knowledge of the interaction of synoptic and local scales. The presence of a surf zone and shoreline defines the coastal-scale response to synoptic forcing through mass and energy conservation at an effectively closed boundary; for example, wave-driven processes in the surf zone respond to sea breeze, cold fronts, and northeasters in a similar manner, even though these processes have vastly different scales (Alvarez-Salgado *et al.*, 2003; Fernandes *et al.*, 2002; Masselink and Pattiaratchi, 1998). The complexity lies in the potential sources of hydrosol components and the multiscale nature of coastal hydrodynamics. This complexity is evident in the open ocean as well (Palacios *et al.*, 2006). Recently developed bio-optical models recognize these interactions and attempt to account for the time dependence of phytoplankton community changes (Shanmugam, 2011). Such an understanding is critical to predicting the occurrence of biological events such as harmful algal blooms in coastal environments.

The hydrodynamic regime concept proposed in this paper can be used to simplify the relationship between atmospheric forcing and marine optics. During the prefrontal phase, synoptic forcing is weak and the hydrosol is dominated by local processes such as phytoplankton blooms and resuspension.

sion of sand at the shoreline. The greatly increased wind speed and resulting larger waves during the frontal regime result in the dominance of synoptic-scale processes, which produce local effects in the nearshore. The hydrodynamics during this phase disrupt the ecosystem and saturate the nearshore with mineral particles. As the postfrontal regime begins, the physical environment weakens substantially, but coastal-scale currents persist for several days. These currents accentuate the prefrontal distribution of the coastal hydrosol by transporting both organic and inorganic material along the coast, as well as offshore.

ACKNOWLEDGMENTS

T.R.K. was supported by the Office of Naval Research through the Naval Research Laboratory 6.1 Core program. R.H.S. was supported by an American Society of Engineering Education Summer Fellowship through the Naval Research Laboratory, and the Coastal Optics project of the Naval Research Laboratory, program element 0601153N of the Office of Naval Research. We also acknowledge the assistance of Alan Weidemann through discussions that contributed substantially to this manuscript. We thank the anonymous reviewers for their constructive comments.

LITERATURE CITED

- Acker, J.; Lyon, P.; Hoge, F.; Shen, S.; Roffer, M., and Gawlikowski, G., 2009. Interaction of Hurricane Katrina with optically complex water in the Gulf of Mexico: interpretation using satellite-derived inherent optical properties and chlorophyll concentration. *IEEE Geoscience and Remote Sensing Letters*, 6, 209–213.
- Alvarez-Salgado, X.A.; Figueiras, F.G.; Perez, F.F.; Groom, S.; Nogueira, E.; Borges, A.; Chou, L.; Castro, C.G.; Momocoffe, G.; Rios, A.F.; Miller, A.E.J.; Frankignoulle, M.; Savidge, G., and Wollast, R., 2003. The Portugal coastal counter current off NW Spain: new insights on its biogeochemical variability. *Progress in Oceanography*, 56, 281–321.
- Babin, M.; Morel, A.; Fournier-Sicre, V.; Fell, F., and Stramski, D., 2003. Light scattering properties of marine particles in coastal and open ocean waters as related to the particle mass concentration. *Limnology and Oceanography*, 48, 843–859.
- Barron, C.N.; Smedstad, L.F.; Rhodes, R.C.; Kara, A.B.; Rowley, C.; Allard, A., and Hurlburt, H.E., 2004. Validation of the 1/8° global Navy Coastal Ocean Model nowcast/forecast system. *Navigators*, Spring 2004, 5–8.
- Binding, C.E.; Bowers, D.G., and Mitchelson-Jacob, E.G., 2005. Estimating suspended sediment concentrations from ocean colour measurements in moderately turbid waters: the impact of variable particle scattering properties. *Remote Sensing of Environment*, 94, 373–383.
- Camenen, B. and Larson, M., 2007. Predictive formulas for breaker depth index and breaker type. *Journal of Coastal Research*, 23, 1028–1041.
- Cao, W.X.; Yang, Y.Z.; Xu, X.Q.; Huang, L.M., and Zhang J.L., 2003. Regional patterns of particulate spectral absorption in the Pearl River estuary. *Chinese Science Bulletin*, 48, 2344–2351.
- Cleveland, J.S., 1995. Regional models for phytoplankton absorption as a function of chlorophyll: a concentration. *Journal of Geophysical Research, Oceans*, 100, 13333–13344.
- Cobb, M.; Keen, T.R., and Walker, N.D., 2008. Modeling the circulation of the Atchafalaya Bay system, part 2: River plume dynamics during cold fronts. *Journal of Coastal Research*, 24, 1048–1062.
- Feng, Z. and Li, C., 2010. Cold-front-induced flushing of the Louisiana bays. *Journal of Marine Systems*, 82, 252–264.
- Fernandes, E.H.L.; Dyer, K.R.; Moller, O.O., and Niencheski, L.F.H., 2002. The Patos Lagoon hydrodynamics during an El Niño event (1998). *Continental Shelf Research*, 22, 1699–1713.
- Ferreira, A.; Garcia, V.M.T., and Garcia, C.A.E., 2009. Light absorption by phytoplankton, non-algal particles and dissolved organic matter at the Patagonia shelf-break in spring and summer. *Deep Sea Research Part I: Oceanographic Research Papers*, 56, 2162–2174.
- Fugate, D.C. and Friedrichs C.T., 2002. Determining concentration and fall velocity of estuarine particle populations using ADV, OBS and LISST. *Continental Shelf Research*, 22, 1867–1886.
- Glenn, S.M. and Grant, W.D., 1987. A suspended sediment stratification correction for combined wave and current flows. *Journal of Geophysical Research, Oceans*, 92, 8244–8264.
- Gould, R.W. and Arnone, R.A., 1997. Remote sensing estimates of inherent optical properties in a coastal environment. *Remote Sensing of Environment*, 61, 290–301.
- Gould, R.W. and Arnone, R.A., 1998. Three-dimensional modelling of inherent optical properties in a coastal environment: coupling ocean colour imagery and *in situ* measurements. *International Journal of Remote Sensing*, 19, 2141–2159.
- Gould, R.W.; Arnone, R.A., and Martinolich, P.M., 1999. Spectral dependence of the scattering coefficient in case 1 and case 2 waters. *Applied Optics*, 38, 2377–2383.
- Gould, R.W.; Arnone, R.A., and Mueller, J.L., 1994. Optical relationships in case-II waters and their application to coastal processes and remote-sensing algorithms. In: *Proceedings of the Second Thematic Conference on Remote Sensing for Marine and Coastal Environments: Needs, Solutions, and Applications*, Volumes I and II, pp. B283–B294.
- Green, R.E.; Gould, R.W., and Ko, D.S., 2008. Statistical models for sediment/detritus and dissolved absorption coefficients in coastal waters of the northern Gulf of Mexico. *Continental Shelf Research*, 28, 1273–1285.
- Haas, K.A. and Svendsen, I.A., 2002. Laboratory measurements of the vertical structure of rip currents. *Journal of Geophysical Research*, 107(C5), 307, doi:10.1029/2001JC000911.
- Haas, K.A. and Warner, J.C., 2009. Comparing a quasi-3D to a full 3D nearshore circulation model: SHORECIRC and ROMS. *Ocean Modelling*, 26, 91–103.
- Haas, K.A.; Svendsen, I.A.; Haller, M.C., and Zhao, Q., 2003. Quasi-three-dimensional modeling of rip current systems. *Journal of Geophysical Research*, 108(C7), 3217, doi:10.1029/2002JC001355.
- Hakvoort, H. and Doerffer, R., 1997. Estimation of specific absorption coefficients of turbid coastal water constituents using the AC-9 and asymptotic attenuation coefficients. In: Ackleson S.G. and Frouin, R. (eds.), *Ocean Optics XIII*. Bellingham, Washington: International Society of Optics and Photonics, pp. 435–439.
- Haltrin, V.I.; Arnone, R.A.; Flynn, P.; Casey, B.; Weidemann, A.D., and Ko, D.S., 2007. Restoring number of suspended particles in ocean using satellite optical images and forecasting particle fields—Art. No. 661504. In: Levin, I.M.; Gilbert, G.D.; Haltrin, V.I., and Trees, C.C. (eds.), *Current Research on Remote Sensing, Laser Probing, and Imagery in Natural Waters*. Bellingham, Washington: SPIE-INT Society Optical Engineering, 61504, doi:10.1117/12.740435.
- Haltrin, V.I.; Shybanov, E.B.; Stavn, R., and Weidemann, A., 1999. Light scattering and backscattering coefficients by quartz particles suspended in seawater. In: *International Geoscience and Remote Sensing Symposium* (Hamburg, Germany), pp. 1420–1422.
- Haus, B.K.; Graber, H.C.; Shay, L.K., and Cook, T.M., 2003. Alongshelf variability of a coastal buoyancy current during the relaxation of downwelling favorable winds. *Journal of Coastal Research*, 19, 409–420.
- Hill, P.S.; Nowell, A.R.M., and Jumars, P.A., 1988. Flume evaluation of the relationship between suspended sediment concentration and excess boundary shear-stress. *Journal of Geophysical Research, Oceans*, 93, 12499–12509.
- Holthuijsen, L.H.; Booij, N., and Bertotti, L., 1996. The propagation of wind errors through ocean wave hindcasts. *Journal of Offshore Mechanics and Arctic Engineering—Transactions of the ASME*, 118, 184–189.

- Hongyan, X.; Zhongfen, Q.; Yijun, H., and Weijun, J., 2007. The absorption of water color components and spectral modes in the Pearl River estuary. *Chinese Journal of Oceanology and Limnology*, 25, 359–366.
- Hou, W.; Gray, D.J.; Weidemann, A.D.; Fournier, G.R.; Forand, J.L., and IEEE, 2007. Automated underwater image restoration and retrieval of related optical properties. In: *IGARSS: 2007 IEEE International Geoscience and Remote Sensing Symposium*, Vols. 1–12—*Sensing and Understanding Our Planet*, (Barcelona, Spain), pp. 1889–1892.
- Hu, C.M.; Muller-Karger, F.E.; Taylor, C.; Carder, K.L.; Kelble, C.; Johns, E., and Heil, C.A., 2005. Red tide detection and tracing using MODIS fluorescence data: a regional example in SW Florida coastal waters. *Remote Sensing of Environment*, 97, 311–321.
- Keen, T.R., 2002. Waves and currents during a winter cold front in the Mississippi Bight, Gulf of Mexico: implications for barrier island erosion. *Journal of Coastal Research*, 18, 622–636.
- Keen, T.R. and Glenn, S.M., 1994. A coupled hydrodynamic bottom boundary-layer model of Ekman flow on stratified continental shelves. *Journal of Physical Oceanography*, 24, 1732–1749.
- Keen, T.R. and Holland, K.T., 2010. The Coastal Dynamics of Heterogeneous Sedimentary Environments: Numerical Modeling of Nearshore Hydrodynamics and Sediment Transport. Report NRL/MR/7320-10-9242. Washington, D.C.: Naval Research Laboratory.
- Keen, T.R. and Slingerland, R.L., 1993. A numerical study of sediment transport and event bed genesis during Tropical Storm Delia. *Journal of Geophysical Research, Oceans*, 98, 4775–4791.
- Keen, T.R. and Stavn, R.H., 2000. Developing a capability to forecast coastal ocean optics: minerogenic scattering. In: *6th International Conference on Estuarine and Coastal Modeling*, (New Orleans, Louisiana, American Society of Civil Engineers), pp. 178–193.
- Keen, T.R.; Stavn, R.H., and Kaihatu, J., 2006. Predicting the effects of physical and optical processes on LIDAR performance at Hamlet's Cove, Florida. AGU, 87(36), *Ocean Sci. Met. Suppl.*, Abstract OS26N-12, Volume 87.
- Keen, T.R.; Stone, G.W.; Kaihatu, J., and Hsu, Y.L., 2003. Barrier island erosion during a winter cold front in Mississippi Sound. In: *Coastal Sediments 2003*. Clearwater Beach, Florida: American Society of Civil Engineers.
- Kirk, J.T.O., 1984. Dependence of relationship between inherent and apparent optical-properties of water on solar altitude. *Limnology and Oceanography*, 29, 350–356.
- Ko, D.S.; Preller, R.H., and Martin, P.J., 2003. An experimental real-time intra-Americas Sea Ocean Nowcast/Forecast System for coastal prediction. In: *Fifth Conference on Coastal Atmospheric and Oceanic Predictions and Processes* (Seattle, Washington), pp. 97–100.
- Kowalczyk, P.; Cooper, W.J.; Whitehead, R.F.; Durako, M.J., and Sheldon, W., 2003. Characterization of CDOM in an organic rich river and surrounding coastal ocean in the South Atlantic Bight. *Aquatic Science*, 65, 381–398.
- Lee, M.E. and Lewis, M.R., 2003. A new method for the measurement of the optical volume scattering function in the upper ocean. *J. Atmos. Ocean. Technol.*, 20, 563–571.
- Martin, P.J.; Smith, S.R.; Posey, P.G.; Dawson, G.M., and Riedlinger, S.H., 2009. Use of the Oregon State University Tidal Inversion Software (OTIS) to Generate Improved Tidal Prediction in the East-Asian Seas. Report NRL/MR/7320-09-9176. Washington, DC: Naval Research Laboratory.
- Masselink, G. and Pattiaratchi, C.B., 1998. The effect of sea breeze on beach morphology, surf zone hydrodynamics and sediment resuspension. *Marine Geology*, 146, 115–135.
- McBride, W.E.; Weidemann, A.D., and Shoemaker, J.T., 1999. Meeting Navy needs with the generic LIDAR model. In: Gilbert, G.D. (ed.), *Airborne and in-Water Underwater Imaging*, Bellingham, Washington: SPIE (International Society for Optical Engineering), pp. 71–82.
- Menon, H.B.; Lotliker, A.A., and Nayak, S.R., 2006. Analysis of estuarine colour components during non-monsoon period through Ocean Colour Monitor. *Estuarine Coastal and Shelf Science*, 66, 523–531.
- Mobley, C.D., 1994. *Light and Water: Radiative Transfer in Natural Waters*. New York: Academic Press, 592p.
- Morey, S.L.; Martin, P.J.; O'Brien, J.J.; Wallcraft, A.A., and Zavala-Hidalgo, J., 2003. Export pathways for river discharged fresh water in the northern Gulf of Mexico. *Journal of Geophysical Research*, 108(C10), 3303, doi:10.1029/2002JC001674.
- Nakata, K. and Doi, T., 2006. Estimation of primary production in the ocean using a physical-biological coupled ocean carbon cycle model. *Environmental Modelling & Software*, 21, 204–228.
- Palacios, D.M.; Bograd, S.J.; Foley, D.G., and Schwing, F.B., 2006. Oceanographic characteristics of biological hot spots in the North Pacific: a remote sensing perspective. *Deep-Sea Research Part II: Topical Studies in Oceanography*, 53, 250–269.
- Peng, F.; Effler, S.W.; O'Donnell, D.; Perkins, M.G., and Weidemann, A., 2007. Role of minerogenic particles in light scattering in lakes and a river in central New York. *Applied Optics*, 46, 6577–6596.
- Power, H.E.; Hughes, M.G.; Aagaard, T., and Baldock, T.E., 2010. Nearshore wave height variation in unsaturated surf. *Journal of Geophysical Research*, 115, C08030, doi:10.1029/2009JC005758.
- Ramath, V.; Feygels, V.; Kopelivich, Y.; Park, J.Y., and Tuell, G., 2010. Predicted bathymetric LIDAR performance of coastal zone mapping and imaging LIDAR (CZMIL). In: Shen, S.S. and Lewis, P.E. (eds.), *Algorithms and Technologies for Multispectral, Hyperspectral, and Ultraspectral Imagery XVI*, Proceedings of SPIE, vol. 7695, Article 769511, doi:10.1117/12.851978.
- Roberts, H.H.; Huh, O.K.; Hsu, S.A.; Rouse, L.J., and Rickman, D., 1987. Impact of cold-front passages on geomorphic evolution and sediment dynamics of the complex Louisiana coast. In: *Coastal Sediments 1987*. New Orleans, Louisiana: American Society of Civil Engineers, pp. 1950–1963.
- Rusu, E., 2010. Modelling of wave-current interactions at the mouths of the Danube. *Journal of Marine Science and Technology*, 15, 143–159.
- Shanmugam, P., 2011. A new bio-optical algorithm for the remote sensing of algal blooms in complex ocean waters. *Journal of Geophysical Research*, 116, C04016, doi:10.1029/2010JC006796.
- Shifrin, K.S., 1983. *Physical Optics of Ocean Water*. New York: American Institute of Physics, 285p.
- Slingerland, R.; Selover, R.W.; Ogston, A.S.; Keen, T.R.; Driscoll, N.W., and Milliman, J.D., 2008. Building the Holocene clinothem in the Gulf of Papua: an ocean circulation study. *Journal of Geophysical Research*, 113, F01S14, doi:10.1029/2006JF000680.
- Snyder, W.A.; Arnone, R.A.; Davis, C.O.; Goode, W.; Gould, R.W.; Ladner, S.; Lamela, G.; Rhea, W.J.; Stavn, R.; Sydor, M., and Weidemann, A., 2008. Optical scattering and backscattering by organic and inorganic particulates in U.S. coastal waters. *Applied Optics*, 47, 666–677.
- Song, H.J.; Ji, R.B.; Stock, C., and Wang, Z.L., 2010. Phenology of phytoplankton blooms in the Nova Scotian Shelf-Gulf of Maine region: remote sensing and modeling analysis. *Journal of Plankton Research*, 32, 1485–1499.
- Stavn, R.H. and Keen, T.R., 2004. Suspended minerogenic particle distributions in high-energy coastal environments: optical implications. *Journal of Geophysical Research, Oceans*, 109, C05005, doi:10.1029/2003JC00209.
- Stavn, R.H. and Richter, S.J., 2008. Biogeo-optics: particle optical properties and the partitioning of the spectral scattering coefficient of ocean waters. *Applied Optics*, 47, 2660–2679.
- Stedmon, C.A.; Markager, S., and Kaas, H., 2000. Optical properties and signatures of chromophoric dissolved organic matter (CDOM) in Danish coastal waters. *Estuarine, Coastal and Shelf Science*, 51, 267–278.
- Stockdon, H.F.; Lillycrop, W.J.; Howd, P.A., and Wozencraft, J.M., 2006. The need for sustained and integrated high-resolution mapping of dynamic coastal environments. *Marine Technology Society Journal*, 40, 90–99.
- Stone, G.W., 1998. Soundside wave-current and beach-nearshore profile adjustment to storms and cold fronts field program along West Ship Island, Mississippi. Report to National Park Service, Vol. II, 20p.

- Stone, G.W. and Wang, P., 1999. The importance of cyclogenesis on the short-term evolution of Gulf coast barriers. *Transactions, Gulf Coast Association of Geological Societies*, pp. 47–48.
- Stramski, D.; Babin, M., and Wozniak, S.B., 2007. Variations in the optical properties of terrigenous mineral-rich particulate matter suspended in seawater. *Limnology and Oceanography*, 52, 2418–2433.
- Stramski, D.; Bricaud, A., and Morel, A., 2001. Modeling the inherent optical properties of the ocean based on the detailed composition of the planktonic community. *Applied Optics*, 40, 2929–2945.
- Tamigneaux, E.; Legendre, L.; Klein, B., and Mingelbier, M., 1999. Seasonal dynamics and potential fate of size-fractionated phytoplankton in a temperate nearshore environment (Western Gulf of St. Lawrence, Canada). *Estuarine Coastal and Shelf Science*, 48, 253–269.
- Wang, G.F.; Cao, W.X.; Yang, Y.Z.; Zhou, W.; Liu, S., and Yang, D.T., 2010. Variations in light absorption properties during a phytoplankton bloom in the Pearl River estuary. *Continental Shelf Research*, 30, 1085–1094.
- Weidemann, A.D.; Fournier, G.R.; Forand, J.L.; Mathieu, P., and McLean, S., 2002. Using a laser underwater camera image enhancer for mine warfare. In: *Applications: What Is Gained?* Stennis Space Center, Mississippi: Naval Research Laboratory p. 6.
- Weidemann, A.D.; Stavn, R.H.; Zaneveld, J.R.V., and Wilcox, M.R., 1995. Error in predicting hydrosol backscattering from remotely-sensed reflectance. *Journal of Geophysical Research, Oceans*, 100, 13163–13177.
- Wozniak, S.B. and Stramski, D., 2004. Modeling the optical properties of mineral particles suspended in seawater and their influence on ocean reflectance and chlorophyll estimation from remote sensing algorithms. *Applied Optics*, 43, 3489–3503.
- Yentsch, C.S. and Ryther, J.H., 1957. Short-term variations in phytoplankton chlorophyll and their significance. *Limnology and Oceanography*, 2, 140–142.
- Yoon, H.-D. and Cox, D.T., 2010. Large-scale laboratory observations of wave breaking turbulence over an evolving beach. *Journal of Geophysical Research*, 115. Doi:10.1029/2009JC005748.
- Zhao, J.; Cao, W.X.; Wang, G.F.; Yang, D.T.; Yang, Y.Z., Sun, Z.H., and Zhou, W., 2009. The variations in optical properties of CDOM throughout an algal bloom event. *Estuarine, Coastal and Shelf Science*, 82, 225–232.

REPORT DOCUMENTATION PAGE				Form Approved OMB No. 0704-0188	
<p>The public reporting burden for this collection of information is estimated to average 1 hour per response, including the time for reviewing instructions, searching existing data sources, gathering and maintaining the data needed, and completing and reviewing the collection of information. Send comments regarding this burden estimate or any other aspect of this collection of information, including suggestions for reducing the burden, to the Department of Defense, Executive Services and Communications Directorate (0704-0188). Respondents should be aware that notwithstanding any other provision of law, no person shall be subject to any penalty for failing to comply with a collection of information if it does not display a currently valid OMB control number.</p> <p>PLEASE DO NOT RETURN YOUR FORM TO THE ABOVE ORGANIZATION.</p>					
1. REPORT DATE (DD-MM-YYYY) 06-12-2012		2. REPORT TYPE Journal Article		3. DATES COVERED (From - To)	
4. TITLE AND SUBTITLE Hydrodynamics on Marine Optics During Cold Fronts at Santa Rosa Island, Florida				5a. CONTRACT NUMBER	
				5b. GRANT NUMBER	
				5c. PROGRAM ELEMENT NUMBER 0601153N	
6. AUTHOR(S) Timothy Keen, Robert Stavn				5d. PROJECT NUMBER	
				5e. TASK NUMBER	
				5f. WORK UNIT NUMBER 73-4261-01-5	
7. PERFORMING ORGANIZATION NAME(S) AND ADDRESS(ES) Naval Research Laboratory Oceanography Division Stennis Space Center, MS 39529-5004				B. PERFORMING ORGANIZATION REPORT NUMBER NRL/JA/7320-11-0812	
9. SPONSORING/MONITORING AGENCY NAME(S) AND ADDRESS(ES) Office of Naval Research 800 N. Quincy St. Arlington, VA 22217-5660				10. SPONSOR/MONITOR'S ACRONYM(S) ONR	
				11. SPONSOR/MONITOR'S REPORT NUMBER(S)	
12. DISTRIBUTION/AVAILABILITY STATEMENT Approved for public release, distribution is unlimited.					
13. SUPPLEMENTARY NOTES					
14. ABSTRACT <p>Observations of optical and hydrodynamic processes were made on the open beach on Santa Rosa Island, Florida, in March 1995. This study focuses on the passage of two cold fronts. The observations have been supplemented by a bio-optical model; a suite of hydrodynamic models to simulate coastal flows forced by waves, tides, local wind, and coastal sea level; and a geo-optical model that predicts scattering by mineral particles resuspended by wave action. These models have been used to examine the interaction of atmospheric forcing and hydrodynamics with respect to the observed marine hydrosol. The optical and hydrodynamic measurements, and the model results, have been used to conceive a cold-front regime model of the hydrosol for open beaches in the Gulf of Mexico. The optical environment during the cold front was determined by three hydrosol phases: (1) a prefrontal steady-state hydrosol consisting of fine resuspended mineral particles, phytoplankton cells, organic detritus, and colored dissolved organic matter; (2) a frontal phase dominated by resuspended mineral particles; and (3) a postfrontal hydrosol containing large phytoplankton, detritus, and fine mineral particles. This concept is useful for identifying the physical processes responsible for observed optical properties. It should be applicable to other regions and types of events.</p>					
15. SUBJECT TERMS <p>nearshore flow, waves, optical scattering, sand resuspension, marine hydrosol</p>					
16. SECURITY CLASSIFICATION OF:			17. LIMITATION OF ABSTRACT UL	18. NUMBER OF PAGES 15	19a. NAME OF RESPONSIBLE PERSON Timothy Keen
a. REPORT Unclassified	b. ABSTRACT Unclassified	c. THIS PAGE Unclassified			19b. TELEPHONE NUMBER (Include area code) 228-688-4950